Surface and atmospheric contributions to passive microwave brightness temperatures for falling snow events

Gail Skofronick-Jackson[1] and Benjamin T. Johnson[2]

Received 30 April 2010; revised 16 September 2010; accepted 23 November 2010; published 29 January 2011.

[1] Physically based passive microwave precipitation retrieval algorithms require a set of relationships between satellite-observed brightness temperatures (TBs) and the physical state of the underlying atmosphere and surface. These relationships are nonlinear, such that inversions are ill-posed especially over variable land surfaces. In order to elucidate these relationships, this work presents a theoretical analysis using TB weighting functions to quantify the percentage influence of the TB resulting from absorption, emission, and/or reflection from the surface, as well as from frozen hydrometeors in clouds, from atmospheric water vapor, and from other contributors. The percentage analysis was also compared to Jacobians. The results are presented for frequencies from 10 to 874 GHz, for individual snow profiles, and for averages over three cloud-resolving model simulations of falling snow. The bulk structure (e.g., ice water path and cloud depth) of the underlying cloud scene was found to affect the resultant TB and percentages, producing different values for blizzard, lake effect, and synoptic snow events. The slant path at a 53° viewing angle increases the hydrometeor contributions relative to nadir viewing channels. Jacobians provide the magnitude and direction of change in the TB values due to a change in the underlying scene; however, the percentage analysis provides detailed information on how that change affected contributions to the TB from the surface, hydrometeors, and water vapor. The TB percentage information presented in this paper provides information about the relative contributions to the TB and supplies key pieces of information required to develop and improve precipitation retrievals over land surfaces.

Citation: Skofronick-Jackson, G., and B. T. Johnson (2011), Surface and atmospheric contributions to passive microwave brightness temperatures for falling snow events, *J. Geophys. Res.*, *116*, D02213, doi:10.1029/2010JD014438.

1. Introduction

[2] Because precipitation is a critical link in the Earth's global water and energy cycles, there is an interest in retrieving precipitation (both rain and snow) in an accurate and consistent fashion on a global basis. The use of satellite observations, such as those available from the upcoming NASA Global Precipitation Measurement (GPM) mission, provides scientists with the necessary spatial and temporal coverage. Crucial for developing physically based precipitation retrieval algorithms is an understanding of the physical relationships between satellite observations of the Earth and the state of the atmosphere and surface within the field of view. These characteristics are often nonlinear, are interrelated, and exhibit complex spatial structures and temporal variations. In general, the lower-frequency channels (10–37 GHz) are more sensitive to surface and absorptive or emissive warming from liquid rain, while the higher-frequency channels (85–874 GHz) are more sensitive to scattering from ice hydrometeors [e.g., *Evans et al.*, 2005]. Sounding channels near the water vapor absorption lines (23, 183, 325, and 448 GHz) respond primarily to the water vapor in the atmosphere and the absorption/emission continuum by water vapor generally increases with frequency. For hydrometeors, the amount, location, composition, and size distribution of the ice (and liquid) particles in the field of view produces varying brightness temperatures (TBs) for different frequencies and permits retrievals of rain rates from 0.2 to 110 mm h^{-1} [*Hou et al.*, 2008].

[3] Precipitation retrievals from space using channels from 10 to 183 GHz have become a mainstay in providing rainfall rate estimates globally as evidenced by the Tropical Rainfall Measuring Mission (TRMM) [e.g., *Kummerow et al.*, 2000], the Advanced Microwave Scanning Radiometer-Earth Observing System (AMSR-E) [*Kawanishi et al.*, 2003], and two Advanced Microwave Sounding Units (AMSU-A and AMSU-B) [e.g., *Ferraro et al.*, 2005]. The Ku band (13 GHz) radar aboard TRMM [*Kummerow et al.*, 2000] and the W band (94 GHz) radar aboard CloudSat [*Stephens et al.*, 2008] provide detailed limited-swath information about the vertical structure of cloud systems. The CloudSat radar responds primarily to cloud particles, light rain, and snow events, similar to that of high-frequency (>90 GHz) passive radiometer channels.

[1]Mesoscale Processes Branch, NASA Goddard Space Flight Center, Greenbelt, Maryland, USA.
[2]Joint Center for Earth Systems Technology, University of Maryland, Baltimore County, Baltimore, Maryland, USA.

Copyright 2011 by the American Geophysical Union.
0148-0227/11/2010JD014438

[4] The conically scanning TRMM and AMSR-E radiometers with channels from ~10 to 89 GHz perform particularly well over oceans when used with physically based precipitation retrieval algorithms [*Lin and Hou*, 2008], while precipitation retrievals over land currently use empirical approaches [*Ferraro et al.*, 2005]. Compared to purely empirical/statistical methods, retrievals based on physical relationships are capable of providing a better understanding of the atmospheric and surface states being estimated given accurate knowledge of the necessary physical-radiometric relationships. Future retrievals over land, such as those for the NASA Global Precipitation Measurement (GPM) mission, are moving toward physically based approaches, since these algorithms have worked well over oceans [e.g., *Kummerow et al.*, 2010].

[5] Recently there has also been an increased interest in estimating both ice phase precipitation particles (e.g., snow and graupel) above the melting layer and ice particles reaching the Earth's surface as snow in order to fully capture the atmospheric water cycle. Ice phase precipitation detection and retrieval algorithms have been reported and shown to be useful in studying near-surface falling snow [*Skofronick-Jackson et al.*, 2004; *Ferraro et al.*, 2005; *Chen and Staelin*, 2003; *Kim et al.*, 2008; *Noh et al.*, 2009]. These falling snow precipitation retrieval algorithms include those that rely on neural networks, statistics, physical relationships, and/or some combination thereof. Millimeter wave and submillimeter wave frequency channels have been exploited in the above approaches.

[6] The passive signature received by satellite radiometers from falling snow events tends to be small with respect to the other contributing factors to the observed brightness temperature. For snowing clouds the surface can contribute >90% of the TB for frequencies below 37 GHz, 20–60% at 166 GHz, and < 30% at higher frequencies. Ideally, physically based retrievals could correct for the surface contributions and eliminate more of the uncertainty due to them. Over oceans it is much easier to determine surface emissivity and temperatures since the surface is generally relatively uniform on the typical scales of passive microwave observations. On the other hand, the emissivity and temperature of the land surface exhibits much stronger variations than ocean, and precipitation (rain or snow) at the surface can exhibit a rapid and strong influence on these quantities as snow accumulates and rain wets soil and vegetation. To determine TB sensitivity to variations in the physical relationships, the influencing factors to the brightness temperatures must be understood and explained. In this paper, we perform straightforward sensitivity analyses of the associated radiometric response for multiple physical realizations of the surface and falling snow events.

[7] One approach that has been used to assist in determining the contributions from these various environmental parameters is Jacobian decomposition [*Voronovich and Gasiewski*, 2004; *Kim et al.*, 2008]. With Jacobians, a tangent linear relationship is created via the use of partial derivatives [e.g., *Voronovich and Gasiewski*, 2004]. The slopes of these partial derivatives can be positive or negative depending on whether the TB increases or decreases in response to changes in the atmospheric variable of interest. As will be shown herein, the disadvantage of the Jacobian is that it does not relate how the change in the atmospheric variable of interest affects the other contributors to the TB values. Other approaches to investigating the sensitivity of TB to atmospheric and surface contributors rely on information theory or optimal estimation theory [e.g., *English*, 1999; *Di Michele and Bauer*, 2006; *Bennartz and Bauer*, 2003; *L'Ecuyer et al.*, 2006]. These techniques are useful because they can be used to select the best possible instrument channels [*Di Michele and Bauer*, 2006], to assess the impact of uncertainties [*L'Ecuyer et al.*, 2006], and to determine the sensitivity of radiances to precipitation and atmospheric profiles [*Bennartz and Bauer*, 2003; *English*, 1999]. Our information content analysis approach employs the direct use of forward radiative TB calculations using the iterative or perturbation method [*Gasiewski*, 1993] as opposed to the more commonly used adding/doubling method.

[8] The advantage of the iterative method for computing passive microwave TBs is that it provides temperature weighting functions that can be used to show the relative contributions from the combined extinction (absorption plus scattering) for the physical cloud parameters of each level in the atmosphere and for the top of the atmosphere and surface boundaries. In this research, the temperature weighting function concept is exploited to analyze the TB sensitivity to the surface, atmospheric hydrometeors, atmospheric water vapor, and other remaining constituents. In the numerical analysis, an estimate of the influence from each of these cloud and surface characteristics to the TB is determined. The key benefit of this type of analysis is the ability to easily separate contributions to TB from the physically distinct and measureable quantities in each layer of the atmospheric scene.

[9] This paper determines the relationships between the key physical variables that influence passive microwave observations. We perform these analyses for selected frequencies ranging from 10 to 874 GHz, consistent with current (e.g., AMSR-E, TRMM, AMSU-B) and planned passive microwave sensors (e.g., GPM, PATH [*National Research Council*, 2007], and submillimeter radiometers [*Buehler et al.*, 2007]). This investigation probes the TB sensitivity over several snow scenarios, such as individual profiles of falling snow, as well as in cloud resolving model (CRM) simulations of three snow events. Vertical atmospheric profile structures from these various cloud classifications are used as input for a robust radiative transfer model [*Skofronick-Jackson et al.*, 2004] where nadir-viewed and 53°-viewed TB are calculated. Section 2 describes the different case profiles, while section 3 provides the procedure for computing TB and decomposing TB into quantitative percentage influence contributions from each source. The percentage analysis results are discussed in section 4, while section 5 provides a comparison between Jacobians and percentages. A summary and conclusions are presented in section 6.

2. Selection of Case Profiles

[10] On the basis of the upcoming GPM mission's interest in the retrievals of falling snow, we emphasize snow events herein. Thus, three CRM simulations of snow events were selected for analysis. The CRM cases included an MM5 model simulation of the 5–6 March 2001 New England

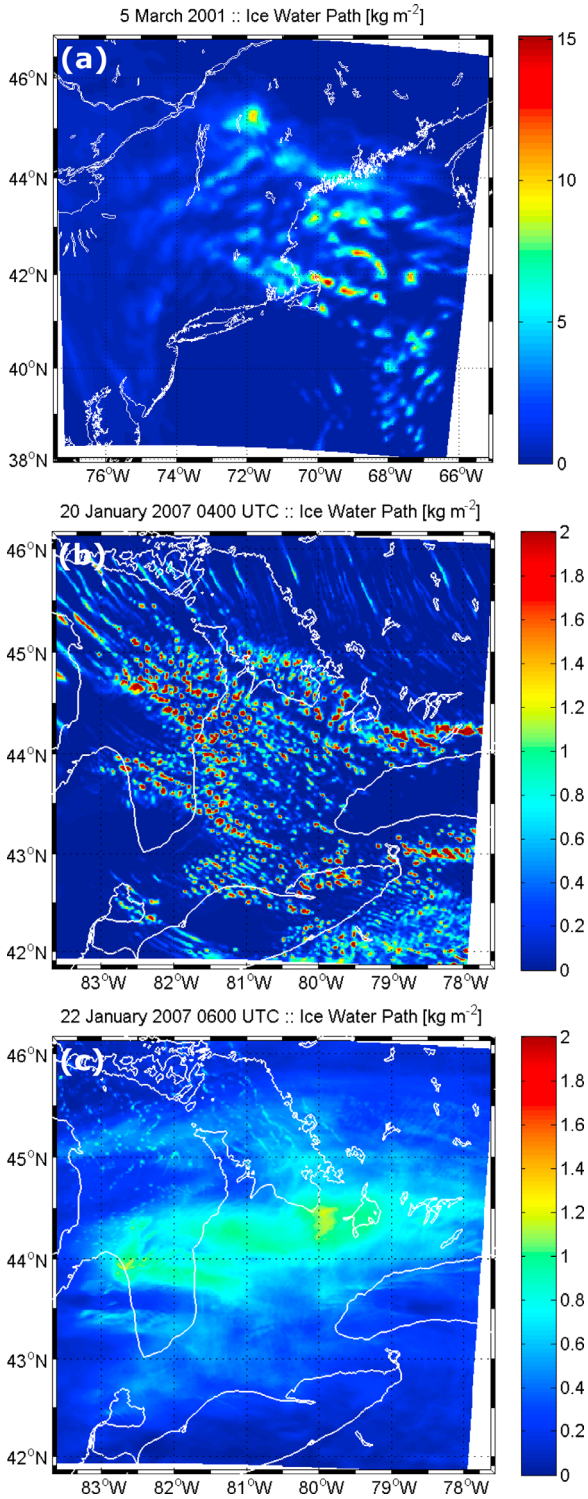

Figure 1. The ice water path (IWP) in kg m^{-2} for (a) the MM5 March 2001 blizzard, (b) the 20 January 2007 lake effect snow storm, and (c) the 22 January 2007 synoptic snow event.

blizzard [*Skofronick-Jackson et al.*, 2004; *Kim et al.*, 2008] and a Weather Research and Forecasting (WRF) multiday simulation of the 20–22 January 2007 winter precipitation events located near the Great Lakes region [*Shi et al.*, 2010]. Figure 1a shows the ice water path (IWP) image of the March 2001 CRM case that deposited up to 75 cm of snow in Vermont. The WRF simulation [*Shi et al.*, 2010] encompassed two events: (1) a shallow cloud lake effect snow at 0400 UTC on 20 January 2007 (Figure 1b) with localized snow accumulations of ~30 cm along the snow bands and (2) a synoptic snow event at 0600 UTC on 22 January 2007 (Figure 1c) with widespread snow accumulations of 5–6 cm. These three events are here denoted as blizzard, lake effect, and synoptic cases. More complicated cases of wet/melting snowfall, multilevel clouds, and 3-D geometry effects were excluded from this analysis.

[11] Three individual cases extracted from the CRM simulations were analyzed. The three snowing cases were determined by selecting the profile with the maximum near-surface snow plus graupel water content (with rainwater path is 0) from all land (not water surface) profiles in the MM5 cloud simulation for the 5–6 March 2001 New England blizzard and similarly for the 20 January 2007 WRF lake effect event and the 22 January 2007 WRF synoptic snow event. These three individual case profiles were located at the latitude, longitude pairs of (42.19°N, 72.09°W), (44.79°N, 83.65°W), (45.11°N, 83.61°W) for the blizzard, lake effect, and synoptic cases, respectively.

[12] The vertical profiles of hydrometeors, temperature, and relative humidity for the three snow cases are shown in Figure 2. The MM5 maximum snow profile case transitions nearly linearly with respect to height from an ice water content (IWC) of 0.0 g m^{-3} at the ~10 km top of the cloud to 0.82 g m^{-3} at the surface. If we assume a Marshall-Palmer [*Marshall and Palmer*, 1948] particle size distribution to convert the surface snow content into a melted rain rate (RR; e.g., RR = $19.9M^{1.2}$), where M is the IWC, the RR for this profile is 15.7 mm hr^{-1} (~6 inches an hour) of a fluffy snow rate (see Table 1) assuming a 1 m s^{-1} vertical velocity and 10-to-1 ratio of fluffy snowpack to melted depth. The snowfall rate will change if the snow is considered to be more or less dense than the commonly assumed 10-to-1 conversion or if the vertical velocity changes. Although hard to distinguish in Figure 2, each of the three profiles contains small amounts of cloud liquid water as prescribed by the CRM models. The surface conditions for the 20 and 22 maximum profile cases are provided in Table 1.

[13] In order to perform the numerical radiative transfer, the information required for each case includes the cosmic background temperature, all surface inputs (surface skin temperature and emissivity), all atmospheric inputs (e.g., vertical profiles of particle size distributions, ice particle shapes, ice-air-water densities, temperature, and water vapor amounts). The simulation cases obtain most of this information as part of the CRM output. Five cloud particles, as specified by the models, are allowed in the radiative transfer calculations: nonprecipitating cloud water, nonprecipitating cloud ice, and precipitating rain, snow, and graupel. The nonprecipitating particles are monodisperse Rayleigh particles with fixed particle size and number density varying to account for the total hydrometeor content per layer. For the hydrometeor particle size distributions, liquid rain particles, although not present in the snow cases would have had spherical shapes and follow the Marshall-Palmer particle size distribution. For the ice particles, randomly oriented nonspherical particles from *Liu*'s [2004] database were used

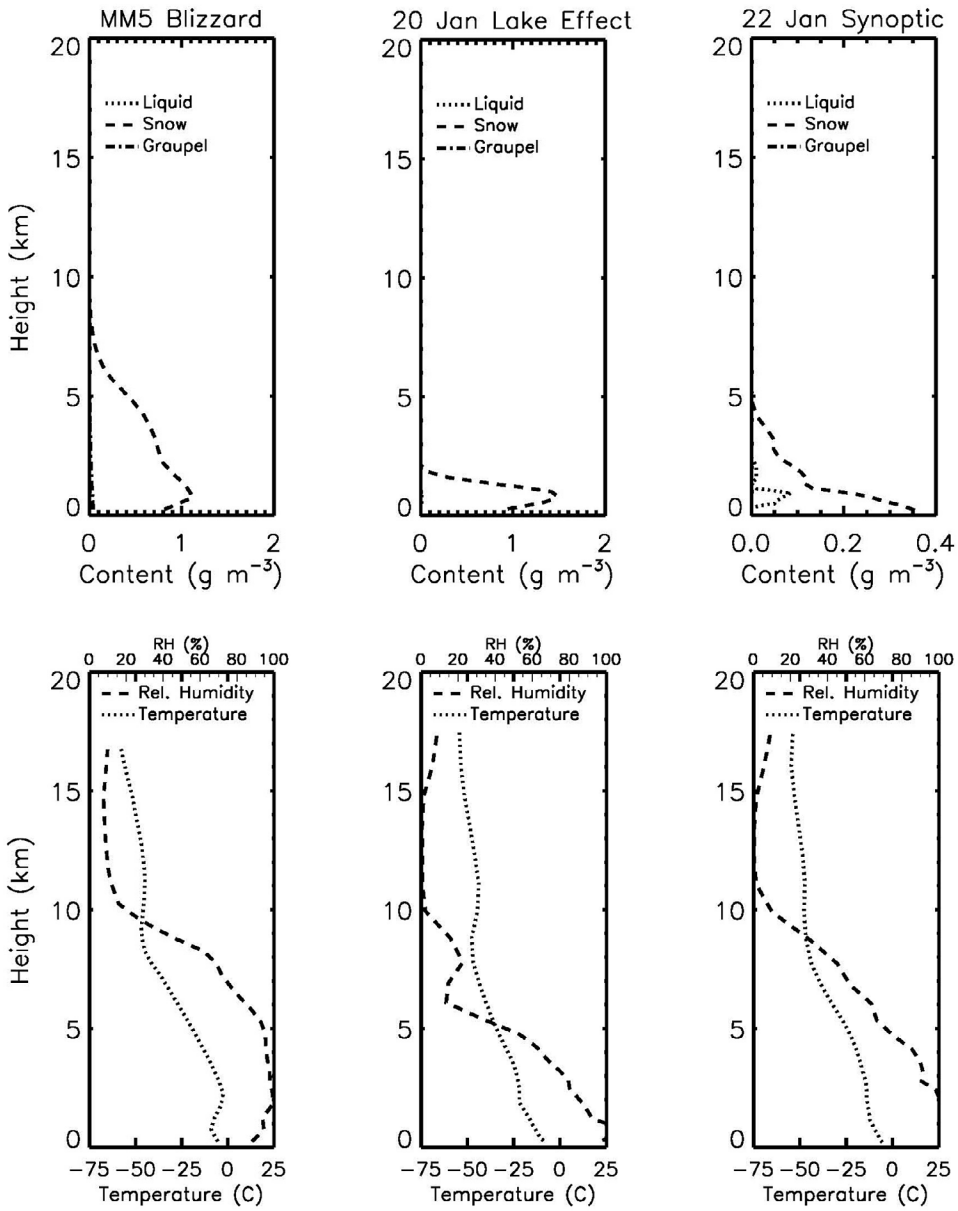

Figure 2. Vertical profiles of (top) hydrometeor liquid and ice water contents and (bottom) temperature and relative humidity for the maximum blizzard, lake effect, and synoptic falling snow profiles.

because frozen spheres are not adequate (as mentioned by *Kneifel et al.* [2010], *Kulie et al.* [2010], *Petty and Huang* [2010], and *Skofronick-Jackson et al.* [2008]). *Liu*'s database provides absorption, scattering, and asymmetry parameters, along with an effective spherical radius over a fixed range of nonspherical shapes. For the snow particles Liu's relatively sparse dendritic shape was assumed (Figure 3a). For denser graupel-like particles the six-sided bullet rosette was assumed (Figure 3b).

[14] In order to preserve and account for all of the IWC in each vertical layer of the cloud resolving model simulations, a particle size distribution (PSD) must be defined and the particle volumes over the PSD integrated to match the model IWC:

$$\mathrm{IWC_{wrf}} = \int_{\min}^{\max} \rho V(D) N(D) dD, \tag{1}$$

Table 1. Surface Conditions for the Selected Falling Snow Profiles

Profile	Land Type	Surface Snow Depth (cm)	Temperature (°C)	Relative Humidity (%)	Melted Snow Rate (mm h^{-1})	Ice Water Path (kg m^{-2})
Blizzard	Mixed forest	1.0	−6	95	16.5	8.9
Lake Effect	Mixed forest	10.0	−5	98	18.7	12.7
Synoptic	Mixed forest	30.0	−3	100	5.7	3.4

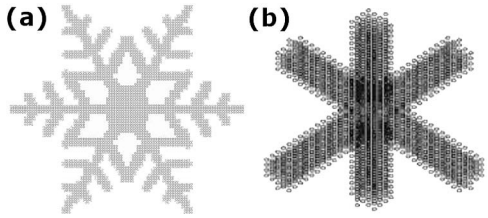

Figure 3. For this work, (a) the dendrite particle shape used for snow particles and (b) the six-sided bullet rosette shape used for graupel particles [from *Liu*, 2004].

where ρ is the density, $V(D)$ is the volume of a sphere with diameter $2 \times r_e$, and $N(D) = N_0 \times \exp(-\Lambda D)$ is the PSD. The PSD used herein allows for 220 particle sizes evenly spaced between the minimum and maximum sizes in *Liu*'s [2004] nonspherical scattering database. Since we do not have the volume of the *Liu* nonspherical particles, we rely on Liu's database to provide the equivalent effective radius (r_e) for a sphere. We use the *Sekhon and Srivastava* [1970] PSD only to set the lambda value (Λ) for the exponential PSD. The N_0 (the number density) is then prescribed by integrating equation (1) over the minimum to maximum particle sizes and forcing integration to match the model IWC. In *Liu*'s [2004] database the minimum and maximum nonspherical (effective radii) sizes are 75 and 12,554 μm (33 and 838 μm) for the dendrites and 50 and 10,000 μm (21 and 1123 μm) for the bullet rosettes. We note that *Kneifel et al.* [2010] approach the limited size range in *Liu*'s [2004] database by requiring that 99% of the snow particles be smaller than Liu's maximum sizes.

[15] A comparison of the absorption and scattering values for the *Liu* [2004] nonspherical particles versus standard spherical particles is provided in Figure 4, which gives representative absorption and scattering coefficients for fixed values of hydrometeor IWC (0.01, 0.1, 0.5, and 0.75 g m^{-3}) for five particle types (rain, Liu dendrites, Liu six-sided bullet rosettes, and, for comparison, fluffy snow spheres (10% ice, 90% air) and solid snow spheres). These contents span the range of contents found in the vertical layers of the selected precipitation cases. Figure 4 shows that liquid rain has a high absorption coefficient across all frequencies, whereas the absorption coefficients for the frozen hydrometeors are 1–3 orders of magnitude smaller. The scattering coefficients for the various hydrometeors are similar for the 0.1, 0.5, and 0.75 g m^{-3} cases (Figures 4b–4d). For the 0.01 g m^{-3} case (Figure 4a), the amount of ice in the frozen layer is too small to cause appreciable scattering whereas the rain does cause an order of magnitude

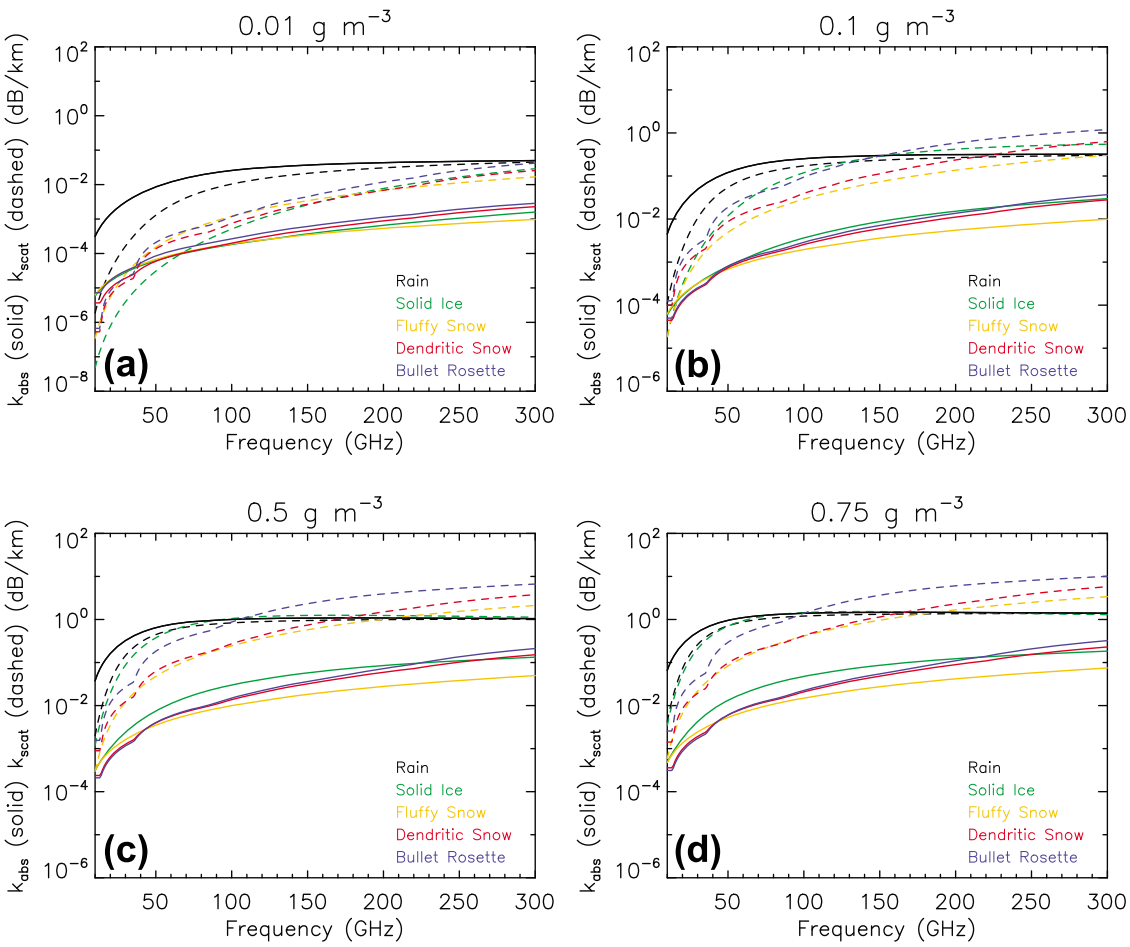

Figure 4. Coefficients for absorption (solid lines) and scattering (dashed lines) for liquid rain, dendritic snow, six-sided bullet rosettes, solid ice spheres, and fluffy ice spheres (10% ice and 90% air) for hydrometeor contents of (a) 0.01 g m^{-3}, (b) 0.1 g m^{-3}, (c) 0.5 g m^{-3}, and (d) 0.75 g m^{-3}.

larger scattering coefficient (but 2 orders of magnitude smaller than the higher-content cases). Note also that the six-sided bullet rosette, our graupel particle, has more scattering than the dendrite particle, our snowflake particle. One would expect that the denser graupel-like particle would generate more scattering than a fluffy snowflake particle with equivalent mass, and helps to justify the choice of these shapes for the snow and graupel particles.

[16] The boundary conditions for the top of the atmosphere and the surface must be prescribed prior to brightness temperature computations and analysis. For all cases, the top of the atmosphere was assumed to be 2.7 K, the cosmic background temperature. The near-surface features of precipitation rate, surface temperature, surface conditions, and relative humidity for these individual cases are presented in Table 1 along with the IWP. For the individual snowing cases the surface was assumed to be mixed forest with varying snow depths as indicated in Table 1.

[17] The surface characteristics for the MM5 and WRF models were provided by the simulations and included land surface temperature, land type, and snow depth. The land type and snow depth of the CRM outputs were used to prescribe the emissivity of the surface. The base emissivities ($\varepsilon_{\text{base}}$) for CRM land type classifications of urban, crop, grass, forest, and water were classified as bare soil, close stubble, close grass, evergreen forest, and water, respectively (taken from [*Hewison*, 2001]). Because the WRF and MM5 models provide snow depth (SD) in centimeters as an output parameter, it was used to adjust the emissivities by the deep dry snow emissivities ($\varepsilon_{\text{snow}}$) provided by *Hewison and English* [1999] using

$$\varepsilon_{\text{adj}} = \frac{\text{SD}}{30}\varepsilon_{\text{snow}} + \left(1 - \frac{\text{SD}}{30}\right)\varepsilon_{\text{base}}, \tag{2}$$

such that there is a linear transition from the base land emissivities to the deep dry snow emissivities for SD from 0 to 30 cm. Here, a 30 cm threshold is use to indicate that all low vegetation is covered by snow. Since the *Hewison and English* [1999] emissivities were derived for localized conditions using aircraft measurements and because generally there is much variability in the emissivity, a random emissivity component within ±0.02 was added to the prescribed emissivities for each profile in the WRF and MM5 domains. Each of the emissivities for the land surface types and deep dry snow are frequency dependent. These TB calculations are performed at the native resolution of the simulations (1 km^2 for WRF, 4 km^2 for MM5) and for each of the 207,000 and 53,000 profiles in the WRF and MM5 domains, respectively.

3. Procedure

[18] In order to determine the percentage influences from the surface, atmospheric hydrometeors, and water vapor components of the case study snowing clouds, a procedure to extract the separate contributions is employed. The procedure requires the use of a forward radiative transfer (FRT) model to compute TB. During the computations, temperature weighting vectors are generated and then used to extract the influences from the atmospheric and surface components.

3.1. Radiative Transfer Calculations

[19] The radiative transfer equations rely on the planar-stratified, multiple scattering based model described by *Skofronick-Jackson et al.* [2004]. For ease in understanding the relationships, nadir brightness temperatures are the focus and are presented first, followed by results at 53°. When the TB values are computed, temperature weighting functions [*Gasiewski*, 1993] are obtained. The brightness temperature at each frequency is the integrated sum over all heights of the product of the weighting vector value and the atmospheric temperature plus the contributions from the ground and cosmic background temperatures:

$$\mathbf{TB} = \int_0^\infty T(z)\mathbf{W}(z)dz = T_0\mathbf{W}_0 + T_{CB}\mathbf{W}_{CB} + \sum_{i=1}^{I} T(z_i)\mathbf{W}_{ALL}(z_i)\Delta z_i, \tag{3}$$

where subscripts 0 (at $z_i = 0$) and CB denote ground surface and cosmic background, respectively. The $T(z_i)$ and $\mathbf{W}_{\text{ALL}}(z_i)$ denote the atmospheric physical temperature in kelvin and a weighting vector value (in km^{-1}), respectively, for level i of the cloud profile that consists of I total levels, and Δz_i is the height increment between level i and level $i - 1$. The brightness temperature contributions (in Kelvin) from level i are the product $T(z_i)\mathbf{W}_{\text{ALL}}(z_i)\Delta z_i$. The weighting vectors depend on the atmospheric cloud constituents at each layer in the atmosphere and include the effects of multiple scattering. The weighting vectors $\mathbf{W}_{\text{ALL}}$, $\mathbf{W}_0$, and $\mathbf{W}_{\text{CB}}$ are defined in *Gasiewski* [1993] where $\mathbf{W}_{\text{ALL}}$ is denoted $\mathbf{W}^{(n)}$.

[20] When plotted (Figure 5), the temperature weighting functions of equation (3) show how the different frequencies of the three individual snow profiles respond to different vertical layers and cloud components (e.g., *Gasiewski* [1993], *Skofronick-Jackson et al.* [2004]). When comparing the weighting functions of the individual snow cases in Figure 5 there are some similarities (e.g., lower frequencies probe the near-Earth atmospheric levels while higher frequencies are more sensitive to the upper altitudes of a cloud). There are also differences due to the amount and distribution of the hydrometeors within the clouds for the various cases. A larger magnitude weight in $\mathbf{W}_{\text{ALL}}(z_i)$ indicates an increased contribution from the atmosphere at those z_i height levels. For example, in Figure 5 for the blizzard case, the magnitude of the nadir-viewed 89 GHz channel is approximately 10 K km^{-1} at the 1–2 km height levels, whereas 166 GHz peaks at 2–4 km with weights of ~25 K km^{-1} and the 183 to 874 GHz channels have larger magnitude peaks (~40 K km^{-1}), but at higher altitudes. Note that the weighting vectors are distributed across the vertical extent of the cloud indicating that TB values are an integrated quantity over the height. Tracing the 166 GHz channel weighting functions across all of the individual cases plotted in Figure 5 shows that the weighting function is highly dependent on IWP, depth of the cloud, and locations of the largest concentrations of IWC.

3.2. Weighting Vector Decomposition and Percentage Influence

[21] The $\mathbf{W}_{\text{ALL}}$ weighting values include the effects (including multiple scattering when present) of every component of the vertical profile (e.g., liquid and frozen pre-

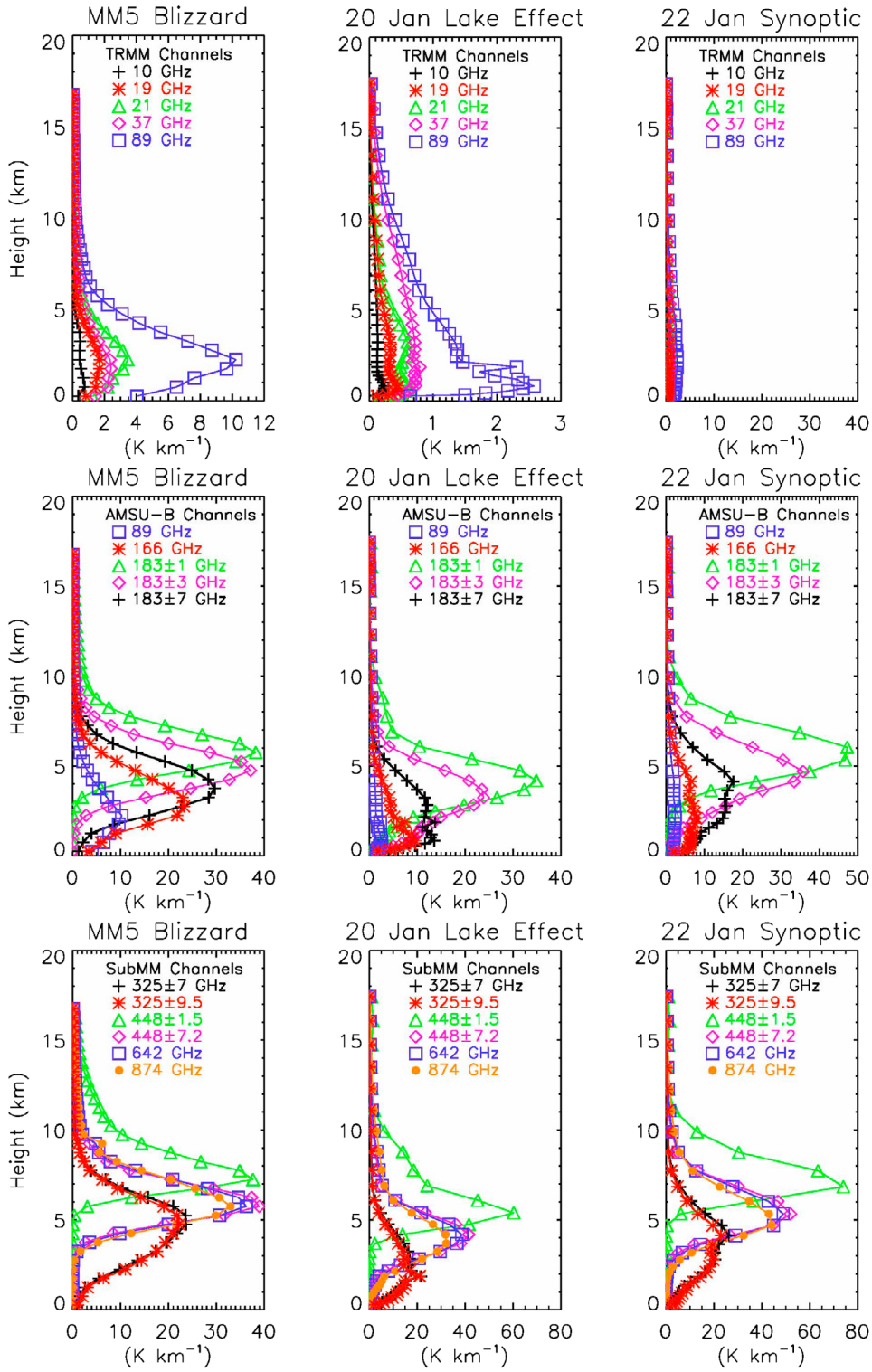

Figure 5. Temperature weighting vectors $W_{ALL}(z_i)T(z_i)$ for nadir-viewed maximum blizzard, lake effect, and synoptic falling snow profiles.

cipitating hydrometeors, nonprecipitating cloud water and cloud ice, water vapor, nitrogen, and oxygen). From equation (3), the surface contribution (in K) to the overall TB value is simply $T_0\mathbf{W}_0$, while the cosmic background contribution is $T_{CB}\mathbf{W}_{CB}$. It is possible to obtain an absorption-only analytical weighting function expressions (e.g., for water vapor in cloud free atmospheres as by *Jackson and Gasiewski* [1995]) in addition to the temperature weighting functions in equation (3); however, when scattering is present analytical weighting functions for components such as precipitating hydrometeors become intractable. Therefore, the approach taken here is to postprocess the temper-

Table 2. Brightness Temperature Values for the Maximum Blizzard, Lake Effect, and Synoptic Falling Snow Profiles for All Hydrometeors Included and for Clear Air Conditions[a]

	Blizzard		Lake Effect		Synoptic	
Frequency	All	CA	All	CA	All	CA
10	245.5	245.7	239.8	239.8	220.5	220.4
19	253.9	256.6	230.2	230.7	191.1	191.1
21	249.1	251.7	231.4	232.0	197.8	198.0
37	250.0	255.4	232.0	232.3	184.5	184.1
89	228.8	260.7	237.0	238.1	201.4	196.3
166	206.6	263.0	227.9	252.2	247.8	242.8
183 ± 1	240.8	242.8	245.1	245.2	243.7	243.7
183 ± 3	238.9	252.3	249.6	250.9	250.9	251.2
183 ± 7	225.1	261.3	244.8	254.8	256.2	256.4
325 ± 7.0	211.9	258.5	246.8	254.3	253.4	255.6
325 ± 9.5	208.1	259.9	244.5	255.1	253.5	256.4
448 ± 1.5	229.1	231.6	234.5	234.5	232.6	232.5
448 ± 7.2	226.9	244.4	243.7	243.9	243.8	244.4
642	227.6	245.0	243.8	244.0	243.7	244.9
874	230.0	246.3	243.9	244.4	243.4	245.8

[a]All, all hydrometeors included. CA, clear air, all hydrometeors zeroed.

ature weighting function $\mathbf{W}_{\mathrm{ALL}}$ (which accounts for the vertical atmospheric and cloud features) by decomposing it into separate quantitative components for studying the relative influences from the precipitating hydrometeors (P), the nonprecipitating cloud water and cloud ice (CWCI), the water vapor (WV), and other contributions (other; e.g., N_2 and O_2) at each height z_i using the following expression (in km^{-1}):

$$\mathbf{W}_{\mathrm{ALL}}(z_i) = \mathbf{W}_{\mathrm{P}}(z_i) + \mathbf{W}_{\mathrm{CWCI}}(z_i) + \mathbf{W}_{\mathrm{WV}}(z_i) + \mathbf{W}_{\mathrm{other}}(z_i). \quad (4)$$

This postprocessing decomposition defines W_P, $\mathbf{W}_{\mathrm{WV}}$, $\mathbf{W}_{\mathrm{CWCI}}$, and $\mathbf{W}_{\mathrm{other}}$ by renormalizing $\mathbf{W}_{\mathrm{ALL}}$ using the various extinction coefficients:

$$\mathbf{W}_{\mathrm{P}}(z_i) = \frac{\mathbf{k}_{\mathrm{Pext}}(z_i)\mathbf{W}_{\mathrm{ALL}}(z_i)}{\mathbf{k}_{\mathrm{ext}}(z_i)}, \quad (5)$$

$$\mathbf{W}_{\mathrm{CWCI}}(z_i) = \frac{\mathbf{k}_{\mathrm{CWCI}}(z_i)\mathbf{W}_{\mathrm{ALL}}(z_i)}{\mathbf{k}_{\mathrm{ext}}(z_i)}, \quad (6)$$

$$\mathbf{W}_{\mathrm{WV}}(z_i) = \frac{\mathbf{k}_{\mathrm{WV}}(z_i)\mathbf{W}_{\mathrm{ALL}}(z_i)}{\mathbf{k}_{\mathrm{ext}}(z_i)}, \quad (7)$$

$$\mathbf{W}_{\mathrm{other}}(z_i) = \frac{[\mathbf{k}_{\mathrm{O2}}(z_i) + \mathbf{k}_{\mathrm{N2}}(z_i)]\mathbf{W}_{\mathrm{ALL}}(z_i)}{\mathbf{k}_{\mathrm{ext}}(z_i)}, \quad (8)$$

where

$$\mathbf{k}_{\mathrm{ext}}(z_i) = \mathbf{k}_{\mathrm{Pext}}(z_i) + \mathbf{k}_{\mathrm{WV}}(z_i) + \mathbf{k}_{\mathrm{CWCI}}(z_i) + \mathbf{k}_{\mathrm{O2}}(z_i) + \mathbf{k}_{\mathrm{N2}}(z_i). \quad (9)$$

The $\mathbf{k}_{\mathrm{Pext}}$ term is the hydrometeor extinction coefficient (the sum of the absorption and scattering coefficients for the rain, snow, and graupel precipitating hydrometeors for layer z_i), $\mathbf{k}_{\mathrm{CWCI}}$ is the sum of the extinction coefficients for cloud water and cloud ice, $\mathbf{k}_{\mathrm{WV}}$ is the extinction coefficient for water vapor, and $\mathbf{k}_{\mathrm{O2}}$ and $\mathbf{k}_{\mathrm{N2}}$ are the extinction coefficients for O_2 and N_2.

[22] Once the temperature weighting vectors have been decomposed into contributions from the surface (surf), cosmic background, atmosphere (precipitating (prec) and nonprecipitating particles), and relative humidity RH they can be used to obtain the influencing value in K of the TB resulting from each of these components:

$$\mathbf{TB}_{\mathrm{surf}} = T_0\mathbf{W}_0, \quad (10)$$

$$\mathbf{TB}_{\mathrm{CB}} = T_{\mathrm{CB}}\mathbf{W}_{\mathrm{CB}}, \quad (11)$$

$$\mathbf{TB}_{\mathrm{prec}} = \sum T(z_i)\mathbf{W}_{\mathrm{P}}(z_i), \quad (12)$$

$$\mathbf{TB}_{CWCI} = \sum T(z_i)\mathbf{W}_{\mathrm{CWCI}}(z_i), \quad (13)$$

$$\mathbf{TB}_{\mathrm{RH}} = \sum T(z_i)\mathbf{W}_{\mathrm{WV}}(z_i). \quad (14)$$

In turn, the percentages are obtained by dividing the above numbers by the total TB defined in equation (3), with the other percentages due to oxygen, nitrogen, and other components.

[23] Note that $\mathbf{k}_{\mathrm{ext}}$ is also used nonlinearly in integrals while computing $\mathbf{W}_{\mathrm{ALL}}$ (which is one reason analytical solutions for scattering weighting functions do not exist). This means that $\mathbf{W}_{\mathrm{P}}$, $\mathbf{W}_{\mathrm{CWCI}}$, $\mathbf{W}_{\mathrm{WV}}$ and $\mathbf{W}_{\mathrm{other}}$ are minimally contaminated by the total $\mathbf{k}_{\mathrm{ext}}$ from the overall constituents; however, the majority of the influencing response is captured for each weighting function component and the renormalization serves to elucidate the relationships between brightness temperatures and the underlying cloud and surface features. Another point to clarify is that a large $\mathbf{k}_{\mathrm{Pext}}$ term can be caused by a large absorption coefficient and/or a large scattering coefficient. In radiative transfer, large scattering coefficients typically result in an upwelling brightness temperature received by a satellite radiometer that is colder than in a nonscattering medium. The advantage of using this weighting function analysis is that it captures the percentage "influence" from large scattering coefficients regardless of the reductions in brightness temperature.

4. Percentage Analysis

[24] Starting with the computed TB values for the three snow cases, Table 2 shows the nadir brightness temperatures when each of the individual profiles has the original hydrometeor profile as seen in Figure 2 and when all hydrometeors are zero (clear air). The brightness temperature values are not provided for the WRF and MM5 cases since they are composed of more than 207,000 and 53,000 profiles, respectively. The TB values associated with the snowing cases in Table 2 show that for frequencies between 10 and 37 GHz, there is a low sensitivity (<5 K difference) between the three snow profiles and their respective clear air brightness temperature values. As the frequency increases, there is greater sensitivity to falling snow particles: At 166 GHz, there is a 60 K difference between clear air and the blizzard case, but the differences are insignificant between clear air and the synoptic snow case. The 183 ± 7 GHz channel are sensitive (~35 K) to the deep (10 km tall) blizzard snow

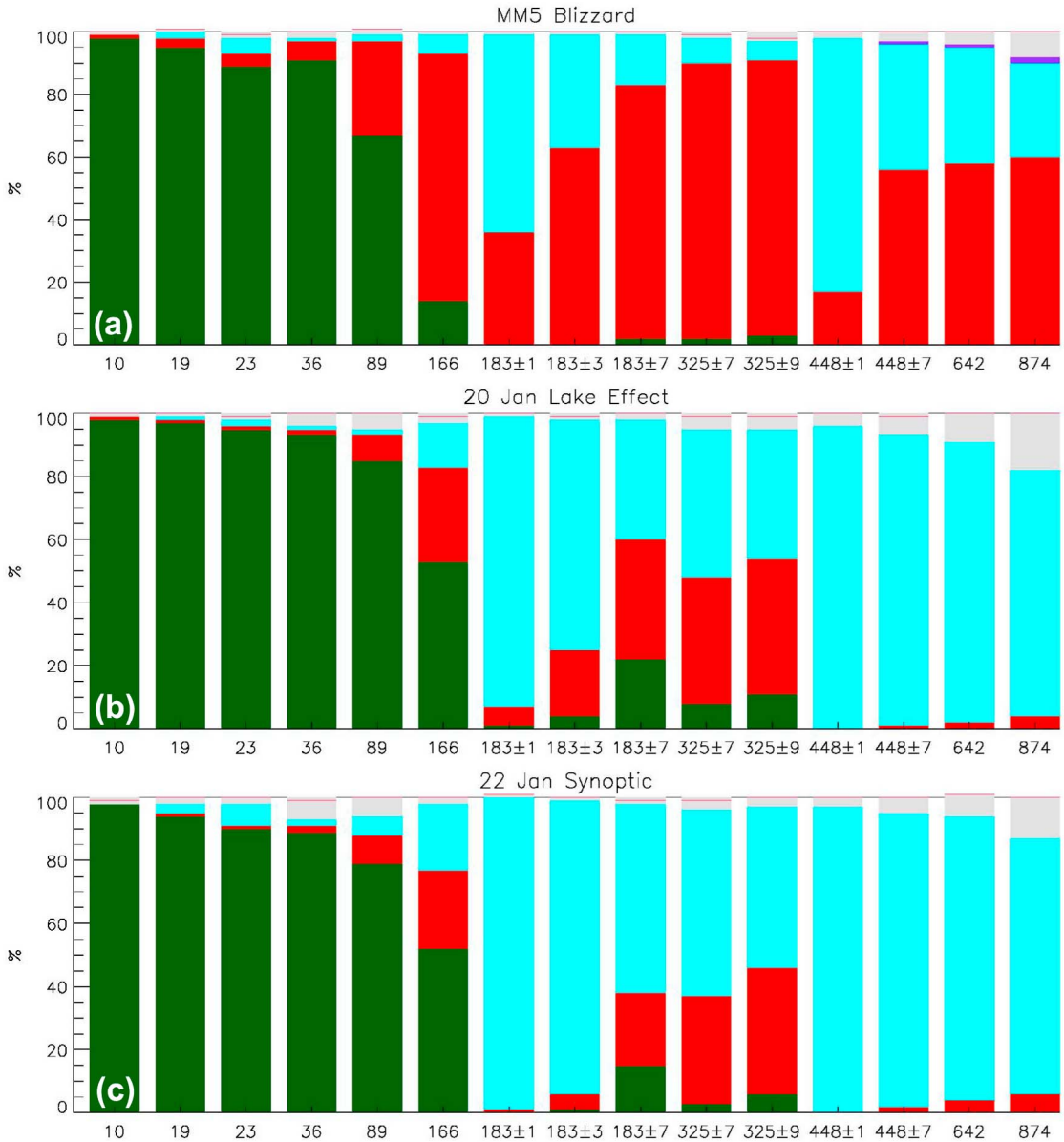

Figure 6. Percentage contributions from the surface (green), hydrometeors (red), the relative humidity (light blue), the cosmic background+cloud water+cloud ice (purple), and from atmospheric oxygen and nitrogen (shaded) to the resultant nadir-viewed brightness temperatures for the maximum (a) blizzard, (b) lake effect, and (c) synoptic falling snow profiles.

clouds. The 325, 642, and 874 GHz channels show strong sensitivity to falling snow (e.g., at 325 GHz the TB shows a nearly 50 K differential between the blizzard snow and its respective clear air case). Between the clear air case and the lake effect snow case for all channels the TB differences are <25 K and the differences are <5 K between the synoptic snow and its clear air profile.

[25] For Figure 6, which shows the percentage contributions for the blizzard, lake effect, and synoptic snow cases as computed using equations (10)–(14), there is a progression of decreasing percentages from the hydrometeors as the snowing rates decrease. Figure 6a (blizzard case), shows the percentages due to hydrometeors range from 20 to 90% (channels 89 to 874 GHz). For the lake effect snow case (Figure 6b) at these frequencies, the hydrometeor percentages are between 5 and 40%, whereas for the synoptic snow case (Figure 6c) the percentages from the hydrometeors drop more. There is a corresponding increase in the percentages from water vapor in the cloud. Not surprisingly the contributions for channels 10 to 89 GHz show a significant percentage (>65%) from the surface. If these were raining profiles instead, then the contribution from the surface would decrease because, as Figure 4 shows, the absorption and scattering of rain is higher than that of frozen particles for frequencies up to 100 GHz. Thus when liquid particles are present, the $\mathbf{k}_{\mathrm{Pext}}$ term in equation (5) is high causing the value of $\mathbf{TB}_{\mathrm{prec}}$ in equation (12) to be elevated. Note that the percentage of the brightness temperature resulting from

Table 3. Percentage Contributions to Brightness Temperatures for the Maximum Blizzard, Lake Effect, and Synoptic Falling Snow Profiles at 53° Viewing and Nadir Viewing Angles[a]

Frequency (GHz)	53° Viewing Angle[b]									Nadir Viewing Angle[c]								
	Blizzard			Lake Effect			Synoptic			Blizzard			Lake Effect			Synoptic		
	Surface	IWP	RH	Surface	IWP	RH	Surface	IWP	RH	Surface	IWP	RH	Surface	IWP	RH	Surface	IWP	RH
10	96	2	0	97	1	0	97	0	0	99	0	0	99	0	0	98	0	0
19	91	5	3	95	2	1	91	1	4	96	0	3	97	0	1	94	0	3
21	83	7	8	92	2	3	85	1	10	90	0	8	95	0	3	90	0	7
37	86	1	1	89	33	1	84	3	3	93	0	3	94	0	1	89	0	3
89	53	41	3	75	13	3	69	13	9	84	0	11	90	0	4	80	0	11
166	10	82	6	38	35	22	35	32	30	47	0	51	76	0	22	55	0	42
183 ± 1	0	31	68	0	1	97	0	0	98	0	0	99	1	0	98	0	0	99
183 ± 3	0	62	36	1	11	86	0	3	96	0	0	99	8	0	90	1	0	98
183 ± 7	1	82	15	11	32	53	5	20	72	8	0	91	40	0	58	16	0	82
325 ± 7.0	2	87	8	4	27	62	1	26	69	1	0	96	22	0	73	6	0	91
325 ± 9.5	3	87	6	6	32	55	2	33	61	3	0	94	30	0	65	10	0	87
448 ± 1.5	0	14	83	0	0	94	0	0	96	0	0	98	0	0	96	0	0	97
448 ± 7.2	0	57	37	0	0	90	0	3	93	0	0	97	0	0	94	0	0	95
642	0	58	33	0	0	86	0	6	89	0	0	95	0	0	90	0	0	93
874	0	59	25	0	1	74	0	11	79	0	0	90	0	0	82	0	0	87

[a]IWP, ice water path. RH, relative humidity.
[b]Horizontal polarity, all hydrometeors included.
[c]Clear air, all hydrometeors zeroed.

the cosmic background is no more than 1.3% (at 10 GHz) and is closer to 0.0–0.3% for the other channels. Furthermore, any percentages less than about 1% (assuming a 150 K TB value) are generally within the instrument noise of current radiometers.

[26] In Table 3, the percentage contributions for the surface, hydrometeors, and relative humidity are provided for radiative transfer calculations at a 53° viewing angle and for clear air at nadir. Note that these percentages do not add to 100% because the contributions from CWCI, O_2, N_2, and cosmic background are not presented in Table 3. Since the land surface component and the randomly oriented snow particles have no polarization dependence, the vertical (V) and horizontal (H) polarization percentages are the same and only the H polarization is shown in Table 3. The 53° viewing angle results show a slight increase in percentages from the hydrometeors due to the increased slant path. The clear air percentages show how the surface and water vapor contribute to the TB in the absence of hydrometeors. These show that window channels are more sensitive to the surface while sounder channels are more sensitive to the water vapor in clear air conditions.

[27] Figure 7 provides percentages for the WRF 20 January 2007 lake effect snow case (Figure 7a) and the 22 January 2007 synoptic snow case (Figure 7b). In order to partition the percentage results for the 207,000 profiles within each of the WRF CRM simulations, an average was taken only over those profiles with IWP of 0.5–1.0 kg m^{-2} (18,160 profiles for 20 January 2007 and 71,420 profiles for 22 January 2007). We can then compare the lake effect case to the synoptic case to illuminate any differences in percentage based on the structure of the vertical profiles. The most noticeable differences are for channels 166, 183, and 325 GHz where the synoptic snow event case is less sensitive to the surface and more sensitive to the snow particles. This is likely because the lake effect events are shallow (3–4 km) clouds, whereas the synoptic events are 6–7 km tall. Thus, despite both plots being averaged over the 0.5–1.0 kg m^{-2} IWPs, the bulk features of the taller clouds impact the weighting functions over a larger vertical extent than the shallower clouds. Clustering of snow event types by bulk feature temperature (T) or humidity (q) profiles may be possible since particle shape and size are driven by temperature and supersaturation levels.

[28] Finally, in Figure 8 the percentages from the MM5 heavy blizzard case are shown. For this case, percentages for an IWP of 0.5–1.0 kg m^{-2} (5325 profiles averaged; Figure 8a) and for an IWP of 9.5–10.0 kg m^{-2} (5 profiles averaged; Figure 8b) were plotted. Since this is a deep snowing cloud (to ~10 km altitude) there is both a greater effect from water vapor in the cloud (for water vapor channels 183, 325, and 448 GHz) and a greater effect from hydrometeors in the profile.

[29] These percentages can be used to analyze which frequencies have the largest response to the various contributing factors. Those channels with larger responses should be used in retrieval procedures. For example, lower-frequency channels should be used for retrievals of surface properties (e.g., soil moisture, wind speed, snow cover, and rain over uniform ocean surfaces). Furthermore, a detailed analysis to determine the thresholds of detection for falling snow cases needs to be undertaken to link TB scattering depressions to the underlying falling snow event characteristics (e.g., cloud top, IWP, particle sizes and shapes, and water vapor profile).

5. Percentage Analysis Compared to Jacobians

[30] Because of the historical use of the Jacobian to investigate the response of brightness temperatures to small changes in input variables [e.g., *Voronovich and Gasiewski*, 2004; *Kim et al.*, 2008], a comparative study between the percentage analysis reported herein and the Jacobian is presented. The comparison is based on the local state of the single blizzard profile shown in Figure 2. (Although not presented herein, the lake effect and synoptic snow events

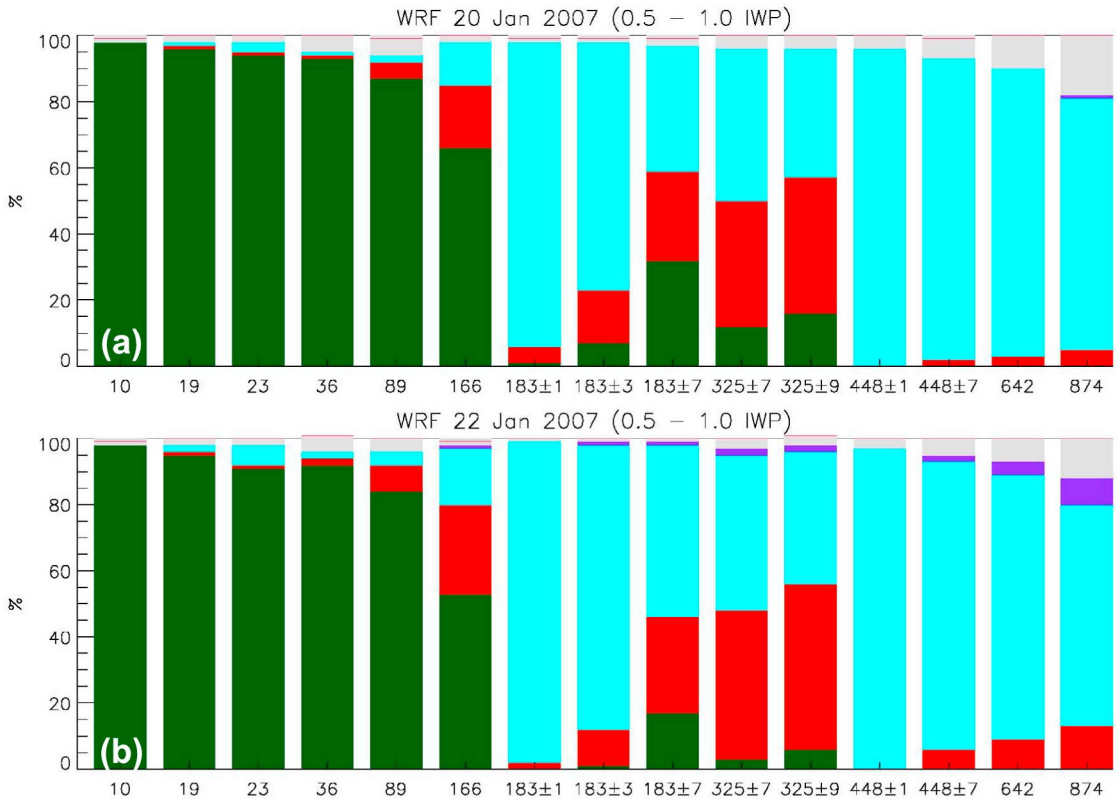

Figure 7. Similar to Figure 6, percentage contributions averaged over IWP of 0.5–1.0 kg m^{-2} for the (a) WRF 20 January 2007 lake effect case and (b) the WRF 22 January 2007 synoptic snow case.

showed similar results with different magnitudes.) Both Jacobians and percentages were computed by varying this blizzard profile's surface emissivity inputs and, separately, the IWP of the profile. As will be shown both the Jacobian and the percentages provide important, yet different, pieces of information about the relationships between the underlying state and the resultant brightness temperatures.

[31] Starting with the analysis for investigations for variations in the IWP to compare Jacobians to the percentages, the blizzard profile is selected and the vertical profile structure is renormalized such that the vertical structure stays the same but the IWP now varies from 0.0, 1.0, …, 10.0 kg m^{-2}. The rest of the blizzard profile remained the same (e.g., surface emissivity, surface temperature, and water vapor profiles). In this way perturbations in changes to the IWP could be investigated using both the percentage analysis as well as the Jacobian process. For computing the Jacobians, the finite difference perturbations from one IWP to the next increment were computed. The resultant percentages, Jacobians, and brightness temperature values are shown in Figure 9. As a note, the positive/negative variations in the 183 ± 1 and 448 ± 1.5 GHz channels were verified and result from small increases/decreases in TB values for these channels.

[32] In Figure 9 the percentages are always positive, but the Jacobians can be negative or positive because the brightness temperature can decrease or increase with an increase in IWP depending on the frequency. As an example, examining 166 GHz, the percentage influence from an increasing IWP causes an increase in the percentages (from 0 to 80% for IWP from 0 to 10 kg m^{-2}). The percentages do not decrease as IWP increases, but they do taper off as saturation occurs. The Jacobian for 0–10 kg m^{-2} at 166 GHz (middle image of Figure 9) shows that the 166 GHz channel has a negative Jacobian value starting at −6 K per IWP from 0 to 1 IWP, down to −8 K from the 1 to 2 IWP change, then transitioning to about a −4 K from IWP of 9 to 10 kg m^{-2}. These Jacobians are all negative because TB decreases when IWP increases. The general presumption is that the decrease in TB (and negative Jacobian values) is due to additional ice scattering from the increased IWP. If, however, we look at the corresponding surface and relative humidity percentage plots associated with IWP 0–10 kg m^{-2} in Figure 10 we see a rather significant drop (50% to 12%) in the percentage from the surface for 166 GHz as IWP increases. This change in surface contribution is caused by an increase in opacity that obscures the surface; this relationship is not captured in the Jacobian analysis. There is also a decrease in the percentage due to the RH as IWP increases. As IWP increases, the interplay between increased scattering, increased atmospheric opacity, and decreased surface emission (reaching the sensor) is not captured in the Jacobian but is identified in the percentage analysis.

[33] Similarly for the emissivity, TB values were computed for all channels using the base blizzard profile (IWP = 8.9 kg m^{-2}) while the surface emissivity (but not surface temperature) varied from emissivities of 0.7 to 0.99 in emissivity increments of 0.03. For the sake of simplicity,

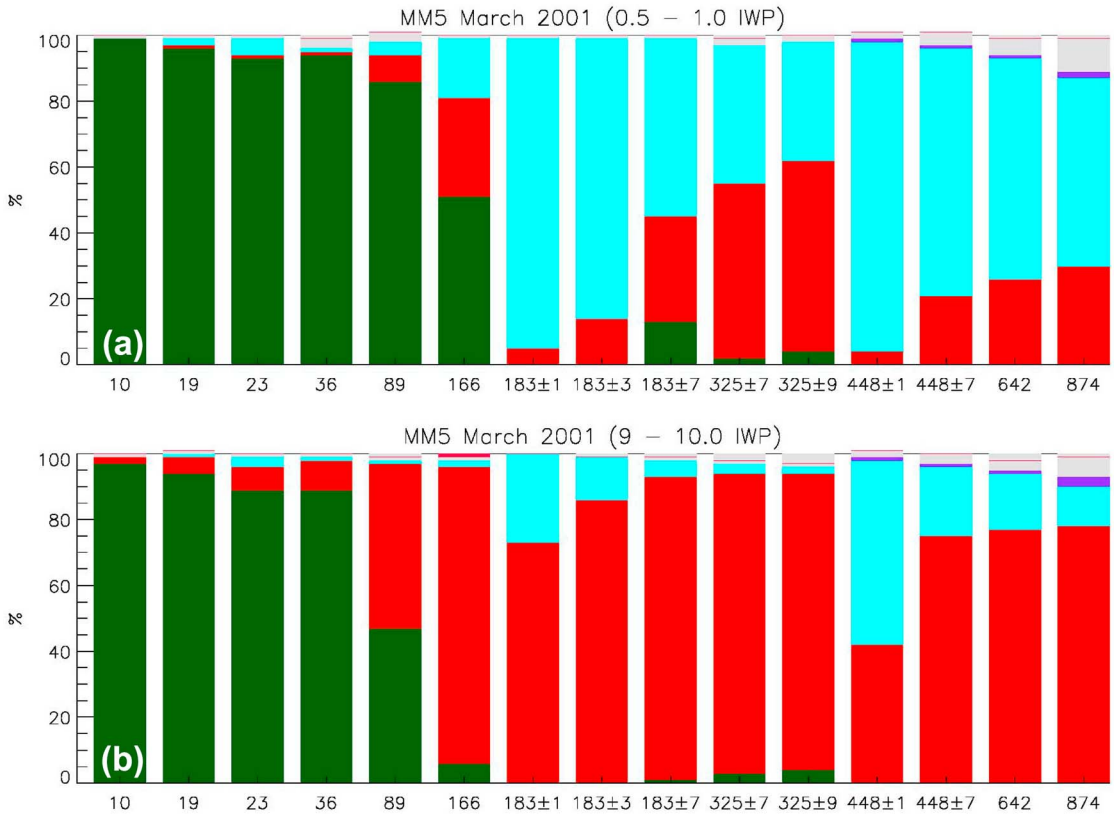

Figure 8. Similar to Figure 6, percentage contributions of a 5 March 2001 snow blizzard MM5 simulation averaged over (a) IWP of 0.5–1.0 kg m^{-2} and (b) IWP of 9.5–10.0 kg m^{-2}.

these emissivities were the same for all channels (which is not the case for the other computations reported herein where emissivity is dependent on frequency). The percentage analysis was performed for each of the 11 steps between 0.7 and 0.99 and Jacobians were computed for subsequent pairs of emissivity (e.g., 0.7, 0.73) computations. The resulting percentages (from the surface), the Jacobians, and the TB are plotted in Figure 11 which shows little variation as the surface emissivity changes except at 89 GHz. For 89 GHz the percentages, Jacobians, and TB values make sense in that the Jacobian changes from 40 to 30 K over the 0.7 to 0.99 emissivity change, while the TB changes 220 to 230 K over the same emissivity range, and the percentage changes from 60 to nearly 70%. While there is little variation over the 0.7 to 0.99 emissivities, the low frequency channels (Figure 11, top) are quite sensitive to the surface with Jacobians of 200 to 250 K per 0.03 emissivity change.

[34] Putting the Jacobian analysis together with the percentage influence information and brightness temperature values provides vital information that helps to interpret the relationships between the underlying physical scene and brightness temperatures. Taken separately, the Jacobian only tells the magnitude and direction of change in the TB, not what parts of the underlying scene contribute more or less due to the changed variable. On the other hand, the percentages show how the brightness temperatures are influenced by the different components of the underlying scene, not the direction and magnitude of the changes in TB values. Including the actual brightness temperature values along with the Jacobians and the percentages completes the picture.

[35] Figures 9–11 are also informative for understanding how potential biases in the cloud resolving models used herein would affect the brightness temperatures and hence also retrievals using such brightness temperatures. For example the MM5 (blizzard case) and WRF (lake effect and synoptic cases) models use different representations for their microphysical parameterization schemes, different forcing fields, and model dynamics [*Kim et al.*, 2008, *Shi et al.*, 2010]. In these cloud resolving models, frozen particle representations generally disagree among the different models as well as compared to observations [*Kneifel et al.*, 2010]. These unknowns and assumptions in the models will transfer into biases in the TB values. It is difficult at this time with limited in situ (and dynamic) constraints to predict the actual biases in the frozen parameterizations in cloud resolving models. Nevertheless, Figures 9–11 show the changes in TB, percentage influence, and Jacobians for small "biases" in the surface emissivity and in the IWP. In Figure 9 an assumed 1 kg m^{-2} bias in the IWP (that could also be attributed to biases in per layer IWC, PSD, and particle shapes) can cause up to an 8–10 K bias in the TB (depending on frequency), and changes of ~25% in the contributions from IWP and RH (Figure 10). For potential biases in emissivities, the lower window channel frequencies are more sensitive (Figure 11, top) that show a 25 K

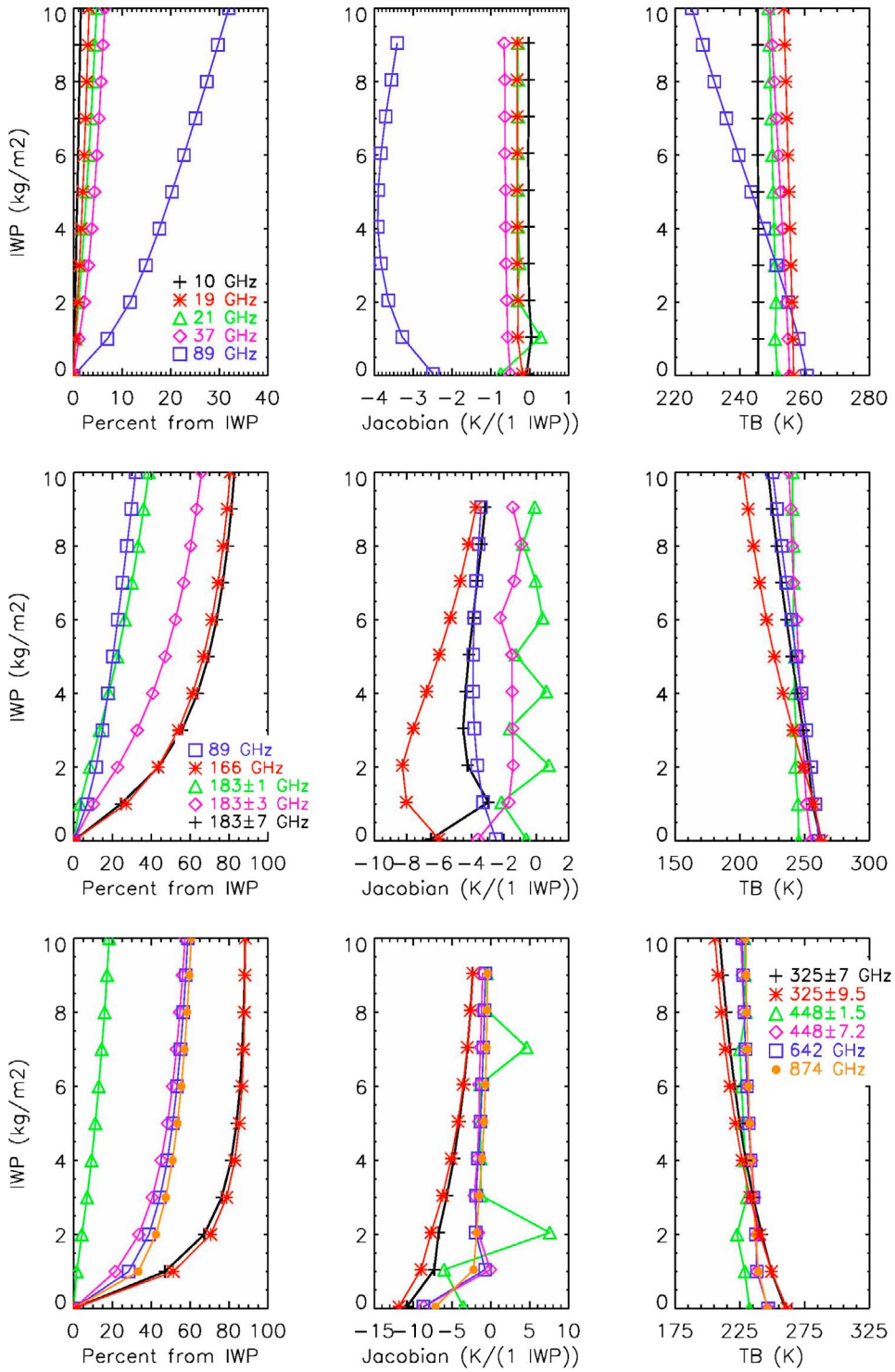

Figure 9. Percentages, Jacobians, and brightness temperatures for ice water paths (IWP) varying from 0.0 to 10.0 kg m^{-2}; (top) 10–89 GHz, (middle) 89–183 ± 7 GHz, and 325 ± 7 to 874 GHz frequency channels.

change in TB for each 0.1 change in emissivity for frequencies <89 GHz.

[36] While a rigorous error analysis makes for a useful future study of this work, the Jacobian, percentage, and TB images in Figures 9–11 point to how changes in emissivity and IWP for a fixed profile affect Jacobians, percentages, and TB. Qualitatively, this information can be used to predict the general errors that might be expected in retrievals due to uncertainty in the emissivity and/or IWP as described above. The images shown in Figures 9–11 are state dependent

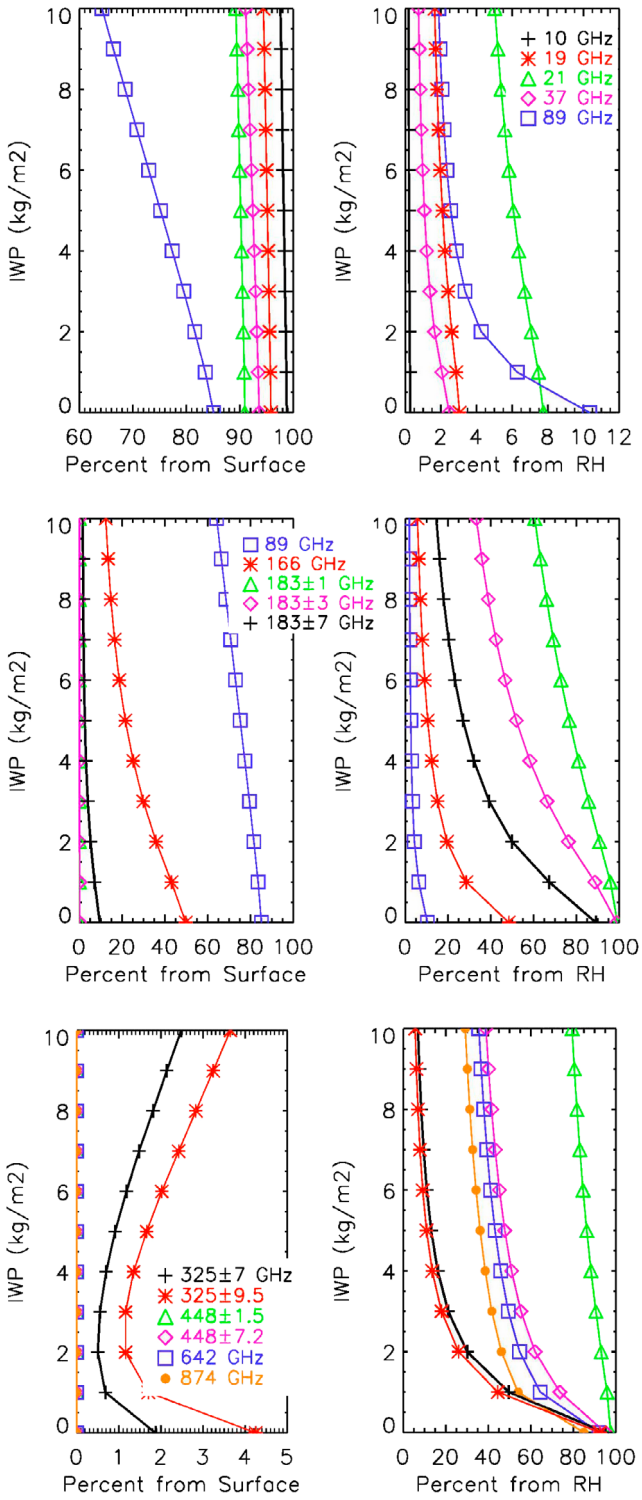

Figure 10. Brightness temperature percentages from the surface and water vapor (RH) for ice water paths (IWP) varying from 0.0 to 10.0 kg m^{-2} corresponding to the cases used in Figure 9.

(MM5 blizzard profile); the use of detailed multiCRM models in the Jacobian and percentage analysis can provide bulk classes of states that can be used to understand uncertainties in the models and their propagation into computed brightness temperature values. In turn these uncertainties can be used as guidelines for retrieval algorithm developers for determining potential errors in the retrievals.

6. Conclusions

[37] This work provides an analysis method to determine the contributions to brightness temperature values from surface emission, atmospheric cloud hydrometeors, cloud water plus cloud ice, water vapor within the vertical profile, the cosmic background, and from O_2 and N_2. This analysis was performed for nadir-viewing and 53° viewing observation channels spanning 10 to 874 GHz, including both window and water vapor sounding channels. These channels are relevant to current and confirmed future missions as well as to channels yet to be approved for a satellite mission. Figures 6–8 show the percentage of the brightness temperature values resulting from the various contributing factors for several individual falling snow profile cases as well as for the average percentages resulting from three cloud resolving model simulations (for a lake effect snow event, a synoptic snow event, and the 2001 New England blizzard). Figures 9–11 compare the percentages to Jacobian analysis results for the same cases. Across all these cases several key points are evident.

[38] 1. Low-frequency channels (<89 GHz) are extremely sensitive to the surface with >65% contribution to the upwelling TB.

[39] 2. Sounding channels have a large contribution from the water vapor in the vertical profile, when there is a limited quantity of hydrometeors in the profile.

[40] 3. Higher-frequency channels, both sounding and window channels, are sensitive to the frozen hydrometeors in the cloud.

[41] 4. The type and vertical structure (IWP and cloud depth) of a snow event (e.g., lake effect, synoptic, and blizzard) in a bulk sense affects the TB and percentages resulting from the surface and hydrometeors.

[42] 5. A slant path at a 53° viewing angle increases the percentage contributions from hydrometeors relative to those from nadir viewing channels.

[43] 6. The percentage analysis and the Jacobians provide two key pieces of information for interpreting the relationships between the underlying scenes and their corresponding TB. Jacobians report the direction and magnitude of change in TB for a change in the underlying scene while the percentages provide information on how the surface, water vapor, and falling snow hydrometeors influence the TB values.

[44] 7. This work can be used to assess the impact of CRM biases on TB and retrievals using our percentage analysis and Jacobians.

[45] 8. Finally, the analysis methods provided here are a useful basis for future work in estimating error uncertainties in retrievals.

[46] This work provides percentage influence values of the sources of brightness temperature signals and shows which channels are sensitive to the various scene components. The relationships between TB and scene are complicated, nonlinear, and vary for each channel and each remotely sensed precipitation event. The number of degrees of freedom in the physical state of precipitation events is

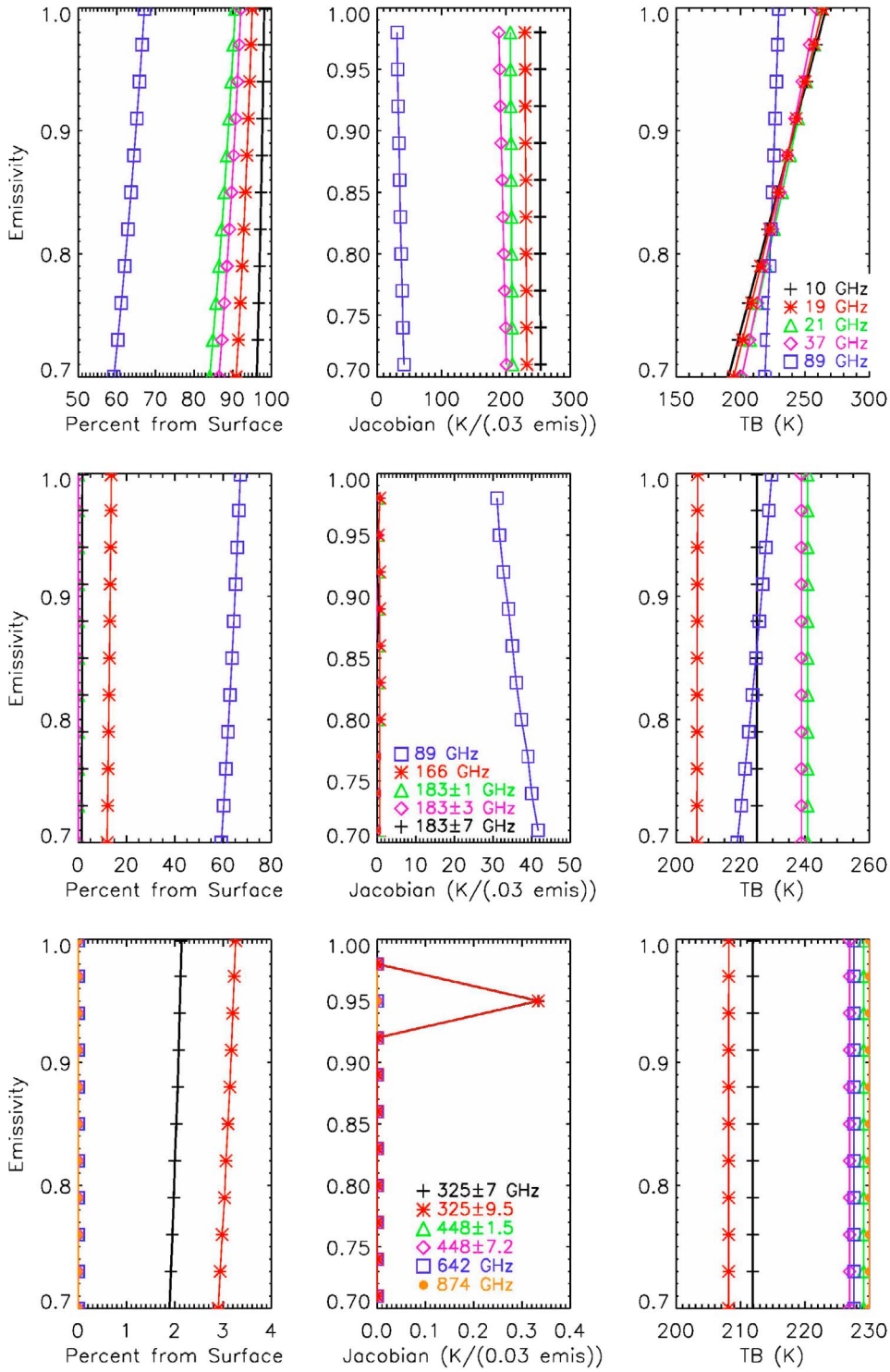

Figure 11. Percentages, Jacobians, and TB for surface emissivities varying from 0.7 to 0.99; (top) 10–89 GHz, (middle) 89–183 ± 7 GHz, and (bottom) 325 ± 7 to 874 GHz frequency channels.

larger than the degrees of freedom available from remotely sensed observations (for current and near-future platforms). Thus, for retrievals over land that are physically based, ancillary data will be extremely useful in reducing the unknowns and assumptions. Primarily, information about the surface emission as well as vertical temperature and water vapor profiles is needed. Since surface emission plays a large role in the typical frequencies used for precipitation sensors (10 to 183 GHz), future work should focus on obtaining realistic and validated surface emission globally as concurred by *Noh et al.* [2009]. Nevertheless, the results presented herein are useful for retrieval algorithm development for upcoming missions such as GPM and PATH, especially over land surfaces and for falling snow events.

[47] **Acknowledgments.** W.-K. Tao and his team are thanked for generating and providing the WRF model simulation and Dong-Eon Chang is thanked for the MM5 simulation. We thank Gousheng Liu for providing the nonspherical ice particle scattering database. We also thank our anonymous reviewers for constructive comments that greatly improved this paper. This work was supported by Ramesh Kakar at NASA Headquarters through Precipitation Measurement Mission funding.

References

Bennartz, R., and P. Bauer (2003), Sensitivity of microwave radiances at 85–183 GHz to precipitating ice particles, *Radio Sci.*, *38*(4), 8075, doi:10.1029/2002RS002626.

Buehler, S. A., et al. (2007), A concept for a satellite mission to measure cloud ice water path, ice particle size, and cloud altitude, *Q. J. R. Meteorol. Soc.*, *133*, 109–128, doi:10.1002/qj.143.

Chen, F. W., and D. H. Staelin (2003), AIRS/AMSU/HSB precipitation estimates, *IEEE Trans. Geosci. Remote Sens.*, *41*, 410–417, doi:10.1109/TGRS.2002.808322.

Di Michele, S., and P. Bauer (2006), Passive microwave radiometer channel selection based on clouds and precipitation information content, *Q. J. R. Meteorol. Soc.*, *132*, 1299–1323, doi:10.1256/qj.05.164.

English, S. J. (1999), Estimation of temperature and humidity profile information from microwave radiances over different surface types, *J. Appl. Meteorol.*, *38*, 1526–1541, doi:10.1175/1520-0450(1999)038<1526:EOTAHP>2.0.CO;2.

Evans, K. F., J. R. Wang, P. E. Racette, G. Heymsfield, and L. Li (2005), Ice cloud retrievals and analysis with the compact scanning submillimeter imaging radiometer and the cloud radar system during CRYSTAL FACE, *J. Appl. Meteorol.*, *44*, 839–859, doi:10.1175/JAM2250.1.

Ferraro, R. R., F. Weng, N. C. Grody, L. Zhao, H. Meng, C. Kongoli, P. Pellegrino, S. Qiu, and C. Dean (2005), NOAA operational hydrological products derived from the advanced microwave sounding unit, *IEEE Trans. Geosci. Remote Sens.*, *43*, 1036–1049, doi:10.1109/TGRS.2004.843249.

Gasiewski, A. J. (1993), Microwave radiative transfer in hydrometeors, in *Atmospheric Remote Sensing by Microwave Radiometry*, edited by M. A. Janssen, pp. 91–144, John Wiley, New York.

Hewison, T. J. (2001), Airborne measurements of forest and agricultural land surface emissivity at millimeter wavelengths, *IEEE Trans. Geosci. Remote Sens.*, *39*, 393–400, doi:10.1109/36.905247.

Hewison, T. J., and S. J. English (1999), Airborne retrievals of snow and ice surface emissivity at millimeter wavelengths, *IEEE Trans. Geosci. Remote Sens.*, *37*, 1871–1879, doi:10.1109/36.774700.

Hou, A. Y., G. Skofronick-Jackson, C. Kummerow, and J. M. Shepherd (2008), Global precipitation measurement, in *Precipitation: Advances in Measurement, Estimation, and Prediction*, edited by S. Michaelides, chap. 6, pp. 131–169, Springer, Berlin, doi:10.1007/978-3-540-77655-0_6.

Jackson, D. M., and A. J. Gasiewski (1995), Millimeter-wave radiometric observations of the troposphere: A comparison of measurements and calculations based on radiosonde and Raman lidar, *IEEE Trans. Geosci. Remote Sens.*, *33*, 3–14, doi:10.1109/36.368227.

Kawanishi, T., T. Sezai, Y. Ito, K. Imaoka, T. Takeshima, Y. Ishido, A. Shibata, M. Miura, H. Inahata, and R. W. Spencer (2003), The Advanced Microwave Scanning Radiometer for the Earth observing system (AMSR-E), NASDA's contribution to the EOS for global energy and water cycle studies, *IEEE Trans. Geosci. Remote Sens.*, *41*, 184–194, doi:10.1109/TGRS.2002.808331.

Kim, M.-J., J. A. Weinman, W. S. Olson, D.-E. Chang, G. Skofronick-Jackson, and J. R. Wang (2008), A physical model to estimate snowfall over land using AMSU-B observations, *J. Geophys. Res.*, *113*, D09201, doi:10.1029/2007JD008589.

Kneifel, S., U. Löhnert, A. Battaglia, S. Crewell, and D. Siebler (2010), Snow scattering signals in ground-based passive microwave radiometer measurements, *J. Geophys. Res.*, *115*, D16214, doi:10.1029/2010JD013856.

Kulie, M. S., R. Bennartz, T. J. Greenwald, Y. Chen, and F. Weng (2010), Uncertainties in microwave properties of frozen precipitation: Implications for remote sensing and data assimilation, *J. Atmos. Sci.*, *67*, 3471–3487, doi:10.1175/2010JAS3520.1.

Kummerow, C., et al. (2000), The status of the Tropical Rainfall Measuring Mission (TRMM) after two years in orbit, *J. Appl. Meteorol.*, *39*, 1965–1982, doi:10.1175/1520-0450(2001)040<1965:TSOTTR>2.0.CO;2.

Kummerow, C. D., S. Ringerud, S. Crook, D. Randel, and W. Berg (2010), An observationally generated a-priori database for microwave rainfall retrievals, *J. Appl. Meteorol. Climatol.*, doi:10.1175/2010JTECHA1468.1, in press.

L'Ecuyer, T. S., P. Gabriel, K. Leesman, S. J. Cooper, and G. L. Stephens (2006), Objective assessment of the information content of visible and infrared radiance measurements for cloud microphysical property retrievals over the global oceans, Part I: Liquid clouds, *J. Appl. Meteorol. Climatol.*, *45*, 20–41, doi:10.1175/JAM2326.1.

Lin, X., and A. Y. Hou (2008), Evaluation of coincident passive microwave rainfall estimates using TRMM PR and ground-based measurements as references, *J. Appl. Meteorol. Climatol.*, *47*, 3170–3187, doi:10.1175/2008JAMC1893.1.

Liu, G. (2004), Approximation of single scattering properties of ice and snow particles for high microwave frequencies, *J. Atmos. Sci.*, *61*, 2441–2456, doi:10.1175/1520-0469(2004)061<2441:AOSSPO>2.0.CO;2.

Marshall, J. S., and W. M. Palmer (1948), The distribution of raindrops with size, *J. Meteorol.*, *5*, 165–166.

National Research Council (2007), *Earth Science and Applications From Space*: *National Imperatives for the Next Decade and Beyond*, 428 pp., Natl. Acad. Press, Washington, D. C.

Noh, Y.-J., G. Liu, A. S. Jones, and T. H. Vonder Haar (2009), Toward snowfall retrieval over land by combining satellite and in situ measurements, *J. Geophys. Res.*, *114*, D24205, doi:10.1029/2009JD012307.

Petty, G. W., and W. Huang (2010), Microwave backscatter and extinction by soft ice spheres and complex snow aggregates, *J. Atmos. Sci.*, *67*, 769–787, doi:10.1175/2009JAS3146.1.

Sekhon, R. S., and R. C. Srivastava (1970), Snow size spectra and radar reflectivity, *J. Atmos. Sci.*, *28*, 944–983.

Shi, J. J., et al. (2010), WRF simulations of the 20–22 January 2007 snow events over eastern Canada: Comparison with in situ and satellite observations, *J. Appl. Meteorol. Climatol.*, *49*, 2246–2266, doi:10.1175/2010JAMC2282.1.

Skofronick-Jackson, G., M.-J. Kim, J. A. Weinman, and D. E. Chang (2004), A physical model to determine snowfall over land by microwave radiometry, *IEEE Trans. Geosci. Remote Sens.*, *42*, 1047–1058, doi:10.1109/TGRS.2004.825585.

Skofronick-Jackson, G., A. Heymsfield, E. Holthaus, C. Albers, and M.-J. Kim (2008), Nonspherical and spherical characterization of ice in Hurricane Erin for wideband passive microwave comparisons, *J. Geophys. Res.*, *113*, D06201, doi:10.1029/2007JD008866.

Stephens, G. L., et al. (2008), The CloudSat mission: Performance and early science after the first year of operation, *J. Geophys. Res.*, *113*, D00A18, doi:10.1029/2008JD009982.

Voronovich, A. G., and A. J. Gasiewski (2004), A fast multistream scattering-based Jacobian for microwave radiance assimilation, *IEEE Trans. Geosci. Remote Sens.*, *42*, 1749–1761, doi:10.1109/TGRS.2004.830637.

B. T. Johnson, Joint Center for Earth Systems Technology, University of Maryland, Baltimore County, 5523 Research Park Dr., Ste. 320, Baltimore, MD 21228, USA. (Benjamin.T.Johnson@nasa.gov)

G. Skofronick-Jackson, Mesoscale Processes Branch, NASA Goddard Space Flight Center, Code 613.1, Building 33, Room A416, Greenbelt, MD 20771, USA. (Gail.S.Jackson@nasa.gov)